

# Insights into the Overcharge-Induced Failure Mechanism of Lithium–Sulfur Batteries

Shungui Deng, Mohammad Jafarpour, Frank Nüesch, Chuanfang Zhang,\* and Jakob Heier\*

In the pursuit of durable lithium–sulfur (Li–S) batteries, considerable research has been devoted to extending cycle life by developing advanced cathode materials. However, there exists a common overcharging problem which leads to the dysfunction of Li–S batteries but has been largely overlooked. This study systematically investigates the overcharging failure and its underlying mechanisms. Experimental results reveal that failure comes from a soft internal short circuit (ISCs) caused by excessive lithium dendrite growth, primarily driven by the sulfur cathode rather than the lithium anode. Electrochemical processes during

overcharging are examined, revealing the generation of a specific by-product. By analyzing the structural properties of the sulfur cathode such as topography and pore connectivity, and through combined experiments and theoretical simulations, the complex mechanisms through which the cathode influences lithium dendrite growth are elucidated. Finally, an effective "interlayer" strategy is proposed to mitigate the overcharging failure. This work sheds light on the overcharging mechanisms and emphasizes the critical importance of cathode design in improving the safety and reliability of Li–S batteries.

## 1. Introduction

Lithium–sulfur (Li–S) batteries hold great promise as a candidate for next-generation energy storage solutions, offering a combination of cost-effective materials and exceptional potential for achieving high energy density.<sup>[1]</sup> The theoretical gravimetric energy density reaches  $\approx 2500 \text{ Wh kg}^{-1}$  calculated from active materials, with current claims of over  $450 \text{ Wh kg}^{-1}$  at the cell level in recent research.<sup>[2]</sup> However, their cycle life is often limited by the so-called "shuttle effect" and the inherently poor electrical conductivity of sulfur. These factors contribute to the formation and accumulation of inactive sulfur ("dead sulfur"), ultimately leading to battery failure. To mitigate rapid capacity decay, numerous strategies have been developed, such as designing porous sulfur hosts with high surface areas and strong lithium polysulfide adsorption capabilities, as well as the introduction of catalysts or mediators to significantly enhance

the electrochemical reaction efficiency.<sup>[3]</sup> In recent years, substantial progresses have been made in the development of advanced cathode materials for reliable and practical Li–S batteries.<sup>[4]</sup>

In practical battery testing, however, another failure mode may emerge. This failure is independent of the well-known "shuttle effect" and occurs specifically during the charging phase. As indicated in Figure 1a and S1, S2, Supporting Information, sudden voltage drops and overcharging behavior can be observed in the voltage–capacity profile. The batteries exhibit uncontrolled current–voltage behavior, with random fluctuations that can persist indefinitely without reaching the cutoff voltage. This issue may occur as early as the first cycle or emerge only after extended cycling. At higher loadings, this phenomenon becomes more frequent and increasingly problematic.

Although this phenomenon has received limited attention from researchers, the underlying interpretations are still controversial. Some suggest that the overcharging phenomenon is related to the sulfur cathode kinetics and uneven formation of  $S_8$ ,<sup>[5]</sup> while another source associates it to internal short circuits (ISCs) in the battery.<sup>[6]</sup> In the research on Li-ion battery thermal runaway, anomalous voltage drop has also been highlighted in several studies.<sup>[7]</sup> This erratic drop-rise behavior has similarly been attributed to the elusive effects of an ISC. Given the direct use of metallic lithium and dual failure potential due to the highly dynamic conversion reactions at both the lithium metal anode and sulfur cathode, the potential risk of ISC in the Li–S battery could escalate significantly, posing challenges that surpass those encountered in conventional lithium-ion batteries. This underscores the need for dedicated investigations. To ensure future practical applications and prevent cell failure or safety hazards, a systematic and thorough investigation of this overcharging failure phenomenon is crucial.

In this study, a composite of amorphous carbon (SuperP)/sulfur was employed as typical sulfur/carbon (S/C) cathodes for investigation. By analyzing the electrochemical performance and disassembling the cells to examine the electrode materials,

S. Deng, M. Jafarpour, F. Nüesch, J. Heier

Laboratory for Functional Polymers

Swiss Federal Laboratories for Materials Science and Technology (EMPA)

Überlandstrasse 129, CH-8600 Zürich, Switzerland

E-mail: Jakob.heier@empa.ch

S. Deng, M. Jafarpour, F. Nüesch

Institute of Materials Science and Engineering

Ecole Polytechnique Fédérale de Lausanne (EPFL)

Station 12, CH-1015 Lausanne, Switzerland

C. Zhang

College of Materials Science & Engineering

Sichuan University

Chengdu 610065, China

E-mail: chuanfang.zhang@scu.edu.cn

 Supporting information for this article is available on the WWW under https://doi.org/10.1002/batt.202500350

 © 2025 The Author(s). *Batteries & Supercaps* published by Wiley-VCH GmbH. This is an open access article under the terms of the Creative Commons Attribution License, which permits use, distribution and reproduction in any medium, provided the original work is properly cited.

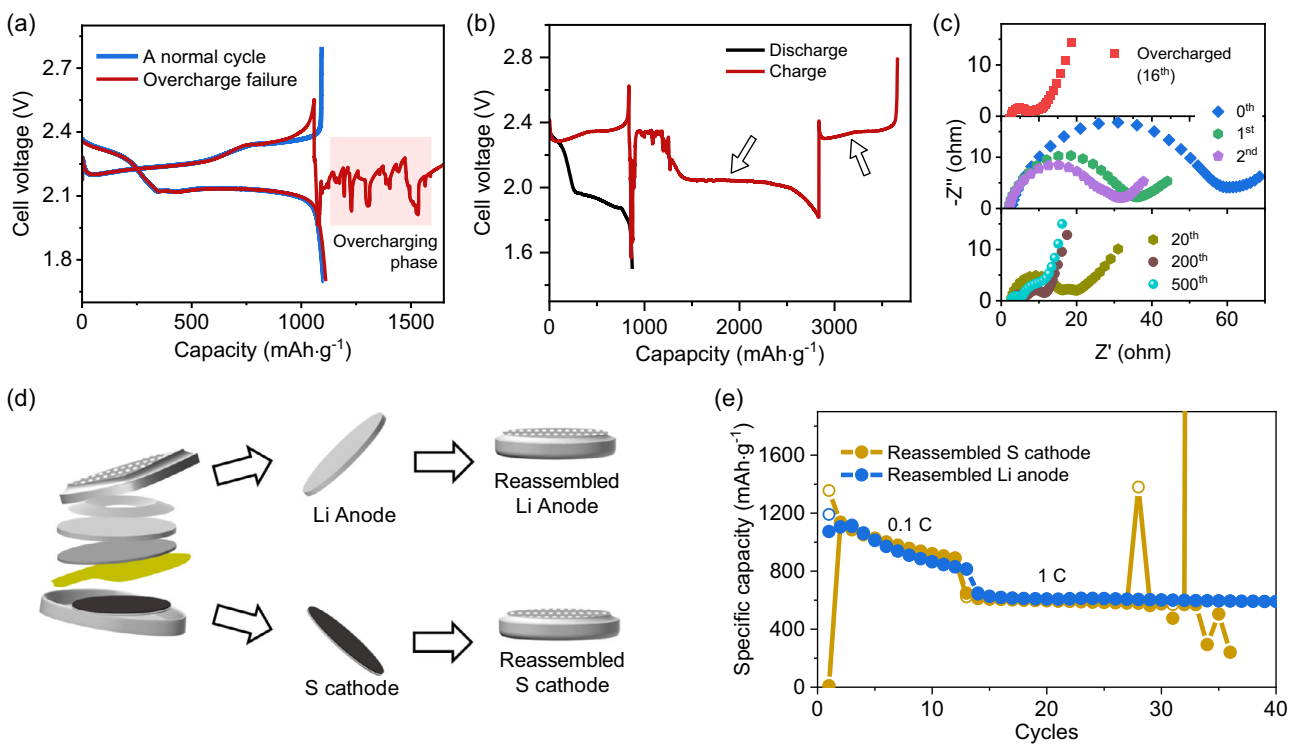


**Figure 1.** a) Typical discharge–charge curves of a normal cycle and an overcharging cycle. b) An overcharging scenario with typical charge and discharge plateaus during overcharging. c) EIS results of an overcharged cell and a normally cycled cell, where the topmost region represents the overcharged condition, while the middle and bottom regions correspond to the first few cycles and prolonged cycles under normal conditions, respectively. d) The sulfur cathode and lithium anode from the overcharged cell were extracted and individually reassembled into new cells. The reassembled S cathode cell used the original sulfur cathode with fresh lithium, separator, and electrolyte; the reassembled anode cell used the original lithium anode with a fresh cathode from a stable batch. e) The electrochemical performance of the reassembled cells.

it was demonstrated that overcharging is caused by ISC due to excessive lithium dendrite growth. This phenomenon, termed a "soft short circuit",<sup>[8]</sup> is characterized by intermittent connections and disconnections between the electrodes. The sulfur cathode is identified as a critical factor driving this growth. Electrochemical processes during the overcharging phase and by-product formation under severe overcharge conditions are further revealed. To explore the role of the sulfur cathode in excessive lithium dendrite growth, it is found that the cathode's topography plays a significant role in influencing lithium deposition on the anode. Furthermore, detailed COMSOL simulations reveal that overcharging is not merely caused by uneven current density from the cathode's surface geometry but results from a more complex mechanism driven by the combined effects of cathode inhomogeneity. Through a comparative study of two cathodes with entirely different structures, deeper insights are gained into how inhomogeneity in the cathode contributes to this process, providing valuable guidance for optimizing cathode design. Finally, an effective strategy is proposed to suppress overcharging and mitigate its detrimental effects, offering a practical approach to enhancing the safety and reliability of lithium-based batteries.

## 2. Results and Discussion

The characteristic features of overcharging are exemplified in Figure 1a. Notably, even in this extreme state, the battery

continues to deliver charging capacity. Subtle clues to the underlying mechanisms can be discerned from the overcharging scenarios (Figure S1, Supporting Information and Figure 1b). The overcharging phase in Figure 1b is marked by the unexpected presence of classical Li–S discharge and charge plateaus. This observation underscores the cathode undergoing oxidation and reduction reactions involving LiPSs. This abnormal reduction reaction occurring during the charging phase can be well explained by the ISC hypothesis, where an influx of electrons from the anode to the cathode induces the reduction of LiPSs.

The same conclusion is supported by the electrochemical impedance spectroscopy (EIS) results in Figure 1c, which shows the Nyquist plots of a representative overcharged battery (top panel, 16th cycle, Figure S2, Supporting Information) and normally cycled batteries from the same electrode batch. As cycling proceeds under normal conditions, the semicircle diameter gradually decreases due to activation at the Li anode (see Figure S3, Supporting Information). Notably, the EIS profile of the overcharged cell resembles that of a normally cycled battery at around the 200th cycle, suggesting a comparable level of activation or fatigue. So, a critical insight is revealed: despite the apparent stagnation in cycle number during overcharging, the cathode undergoes continuous internal redox reactions with countless charge–discharge events, leading to progressive aging and sustained capacity contribution.

It is worth noting that overcharging does not lead to catastrophic failure in all cases. Some cases, such as those shown

in Figure S4, Supporting Information, demonstrate benign behavior where the battery successfully absorbs sudden voltage drops without compromising subsequent cycling performance. The galvanostatic intermittent titration technique (GITT) was employed to segment a typical benign overcharging process, enabling the identification of the short circuit and subsequent self-regulation phases, as illustrated in Figure S5 and S6, Supporting Information. Simultaneously, decomposing the charge polarization into  $\eta_{\text{act}}$ ,  $\eta_{\text{con}}$ , and  $\eta_{\text{ohm}}$  provides critical insights (Figure S7, Supporting Information),<sup>[9]</sup> which represent the activation polarization, concentration polarization, and ohmic polarization, respectively. Figure S8, Supporting Information, reveals the evolution of these internal impedances during the whole stages. It is found that a momentary short circuit disrupts the  $\text{Li}^+$  distribution, resulting in a decrease in  $\eta_{\text{con}}$ , which progressively recovers as the ion distribution adjusts to equilibrium. This recovery process typically takes several to over a dozen hours. Throughout this period,  $\eta_{\text{con}} + \eta_{\text{ohm}}$  remains stable, indicating that the intrinsic reaction kinetics are not affected by the intermittent short circuit.

To identify the underlying cause of overcharging failure, we disassembled affected cells and reassembled the extracted sulfur cathode or lithium anode with fresh counterparts (new lithium/cathode, separator, and electrolyte, Figure 1d). This eliminated the original short-circuit path and isolated the contribution of each electrode. Interestingly, the reassembled cell using the

cycled lithium anode showed stable performance, while the one using the cycled sulfur cathode, though initially normal, eventually exhibited overcharging failure again (Figure 1e). Repeated trials consistently show the same trend, indicating that the root of overcharging failure originates from the faulty sulfur cathode (Figure S9, Supporting Information). Further evidence lies in the observation that some batches of S cathodes show a heightened susceptibility to overcharging, while others rarely exhibit such issues, even though all experiments utilize nominally identical lithium chips as anodes. This batch-dependent variability highlights the S cathode as a focus for targeted investigation into the structural and compositional differences across cathode batches.

To investigate the impact of overcharging failure on the sulfur cathode, we examine the electrode surface by disassembling the batteries. For cells cycled under typical conditions, the sulfur cathode exhibits minimal changes, aside from becoming smoother and cleaner after cycling (Figure 2a–c). In contrast, catastrophic overcharging results in significant alterations. As illustrated in Figure 2d–f, a battery experiencing a severe voltage drop to 0.5–0.7 V during the fifth cycle reveals the formation of a distinctive byproduct that heavily coats the surface of the sulfur cathode. While not all overcharged batteries display such extensive coverage, traces of these dendritic byproducts are consistently observed in other severely overcharged cells (Figure S10,

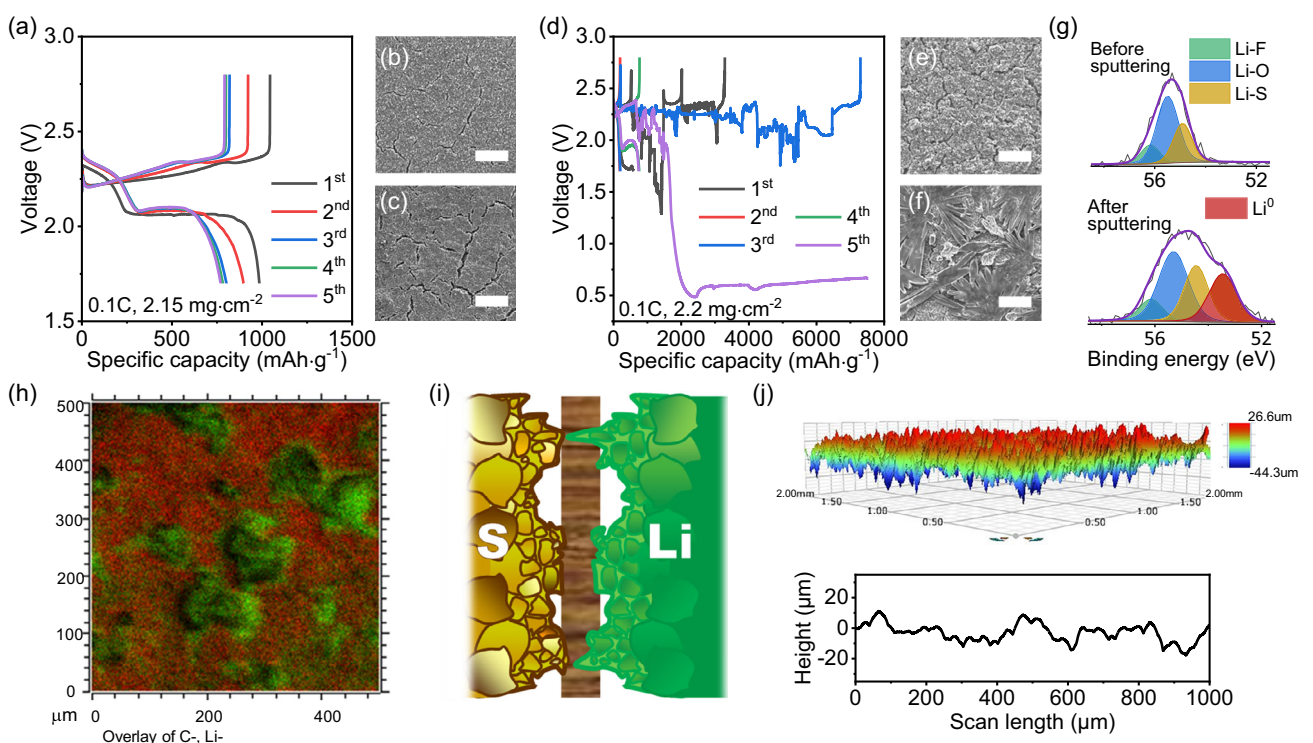


**Figure 2.** a) Electrode cycled under normal conditions and the corresponding cathode surface morphology b) before and c) after cycling. d) Electrode subjected to catastrophic overcharging and the corresponding cathode surface morphology e) before and f) after cycling. The scale bars for (b), (c), (e), and (f) are all 200  $\mu\text{m}$ . g) XPS analysis of the Li 1s spectra for the overcharged S/C cathode, shown both before and after sputtering, where residual lithium salts, electrolyte, and sulfur-related decomposition products (e.g., solid-electrolyte interphase) can contribute to the observed Li-F, Li-O, and Li-S peaks. h) TOF-SIMS overlay mapping of  $\text{Li}^-$  (green) and  $\text{C}^-$  (red) signals in the selected region containing byproduct fragments from an overcharged cell. i) Schematic illustration of how the geometry of the sulfur cathode influences the lithium anode geometry. j) Surface topography measured by a profilometer.

Supporting Information). And the abundance of these byproducts appears to reflect the severity of the overcharging.

Scanning electron microscopy (SEM) images recorded with a concentric backscatter detector show that the byproduct appears darker than its surroundings, indicating the presence of lighter elements, potentially Li (Figure S11, Supporting Information). Energy dispersive spectroscopy (EDS) analysis was conducted to further investigate the element composition. Although Li cannot be directly detected with EDS, the results reveal significant amounts of S and O within the byproduct (Figure S12, Supporting Information). The oxygen is likely attributable to the oxidation of Li. The most compelling evidence comes from X-ray photoelectron spectroscopy (XPS) analysis of the electrode in Figure 2f. As shown in Figure 2g, after sputtering the electrode surface, metallic Li is unequivocally detected on the above overcharged cathode. In contrast, no metallic lithium is observed on the cathode of normally cycled batteries (Figure S13, Supporting Information). This provides direct confirmation that Li dendrite penetration, leading to ISC, is the primary cause of overcharging failure. Supporting this conclusion, visual evidence of suspected Li dendrite penetration was also captured (Figure S14, Supporting Information). Moreover, the spatial distribution of Li and C on the overcharged cathode with by-product fragments is further analyzed by time-of-flight secondary ion mass spectrometry (TOF-SIMS), as shown in Figure 2h and S15, Supporting Information, which clearly reveals that Li is predominantly enriched on the by-product fragments.

For batteries that have experienced catastrophic overcharging, cathode reactivation remains a possibility. As shown in Figure S16a, Supporting Information, the voltage of the failed battery dropped to 0.5 V. After replacing the anode, separator, and electrolyte, the reassembled cell maintained the same low open-circuit voltage (Figure S16b, Supporting Information), indicating that the low potential of the cell originates from the cathode. Since a typical S/C cathode has an equilibrium potential above 2 V, this result also supports that metallic lithium might be deposited on the cathode. In the first cycle after reassembly, virtually no discharge capacity was yielded, indicating that the active material was already in a fully reduced state, primarily  $\text{Li}_2\text{S}$ . Upon charging, the voltage initially rose from 0.5 to 2.6 V without a clear plateau, which likely corresponds to the removal of metallic lithium or other side products generated during overcharging. After this initial stage, the cell transitioned into a typical Li–S charging profile, reflecting the oxidation of  $\text{Li}_2\text{S}$ . Subsequent cycles exhibited normal behavior, although overcharging reappeared under high-rate conditions (Figure S16c, Supporting Information). These results suggest that the cathode remained electrochemically active and was not severely passivated by irreversible by-products. In addition, the overcharged cathode contained a significant amount of reduced  $\text{Li}_2\text{S}$  species, likely constituting part of the by-products. This inference is directly supported by the XPS analysis (Figure S17, Supporting Information), which reveals a predominant  $\text{S}^{2-}$  signal, in sharp contrast to the higher valence sulfur species observed under normal charged conditions, confirming that the by-products indeed contain a considerable amount of reduced lithium sulfide.

The characteristics of sulfur cathodes that contribute to their susceptibility to overcharging have been investigated. Multiple experiments reveal that higher sulfur loadings make overcharging occur more easily, as also noted in earlier studies.<sup>[5,6]</sup> Yet, even with the same loading, sulfur cathodes from different batches still possibly exhibit varying susceptibility to overcharging. Interestingly, initial observations revealed that some cathodes prone to overcharging appeared to exhibit surface protrusions. This led to the hypothesis that surface topography may play a critical role. As illustrated in Figure 2i, it is proposed that protrusions on the cathode surface led to local current density concentration, disrupting the uniformity of  $\text{Li}^+$  migration flux. This uneven flux can further result in a nonuniform current density distribution on the anode, promoting dendrite growth in affected regions. To examine this, we measured the surface topography of a typical S/C cathode using a profilometer, with the results shown in Figure 2j and S18, Supporting Information. The surface roughness is found to be substantial, with peak-to-valley height differences ranging from 30 to 70  $\mu\text{m}$ , while the separator thickness is typically only 25  $\mu\text{m}$ . The impact on surface morphology is also clearly revealed by SEM analysis (Figure S19, Supporting Information). These findings suggest that the cathode morphology may play a critical role in its susceptibility to overcharging.

To visually demonstrate how the topography characteristics of the cathode shape lithium deposition behavior on the anode, a corrugated cathode with well-defined surface irregularities is engineered (Figure 3a,b). Profilometric measurements and cross-sectional imaging confirm these features (Figure 3c and S20, Supporting Information), showcasing a landscape of raised and recessed regions with a height variation of  $\approx 60 \mu\text{m}$ . After cycles, SEM analysis of the lithium anode surface unveils a strikingly similar pattern, echoing the cathode's corrugation with pronounced height variations (Figure 3d-f). Intriguingly, these elevated regions on the lithium anode align directly with the cathode's protrusions, indicating that the morphological imprint on the lithium surface stems from localized deposition rather than mechanical indentation. Detailed observation reveals noticeable lithium grains in the raised areas, whereas the recessed zones retain a surface texture closer to that of pristine lithium (Figure S21, Supporting Information). This distinctive pattern confirms that the cathode's topography plays a notable role in directing lithium plating, inducing an "imprinting effect" that mirrors its own structural contours.

We then simulated the above scenario in COMSOL to explain such preferential Li plating behavior under the classical Nernst–Planck theoretical framework, analyzing the distribution of current density in the electrolyte, as shown in Figure 3g. It is evident that due to the topographical differences on the cathode, elevated areas exhibit significantly higher current density than recessed areas, thereby influencing the anode through localized  $\text{Li}^+$  flux. This suggests that lithium plating at the anode corresponding to the elevated regions on the cathode is more active. Based on this framework, the lithium electrodeposition is simulated. However, the simulation does not reflect the experimental observation. As shown in Figure 3h, the variation in plating thickness at the anode is less pronounced than that observed in the

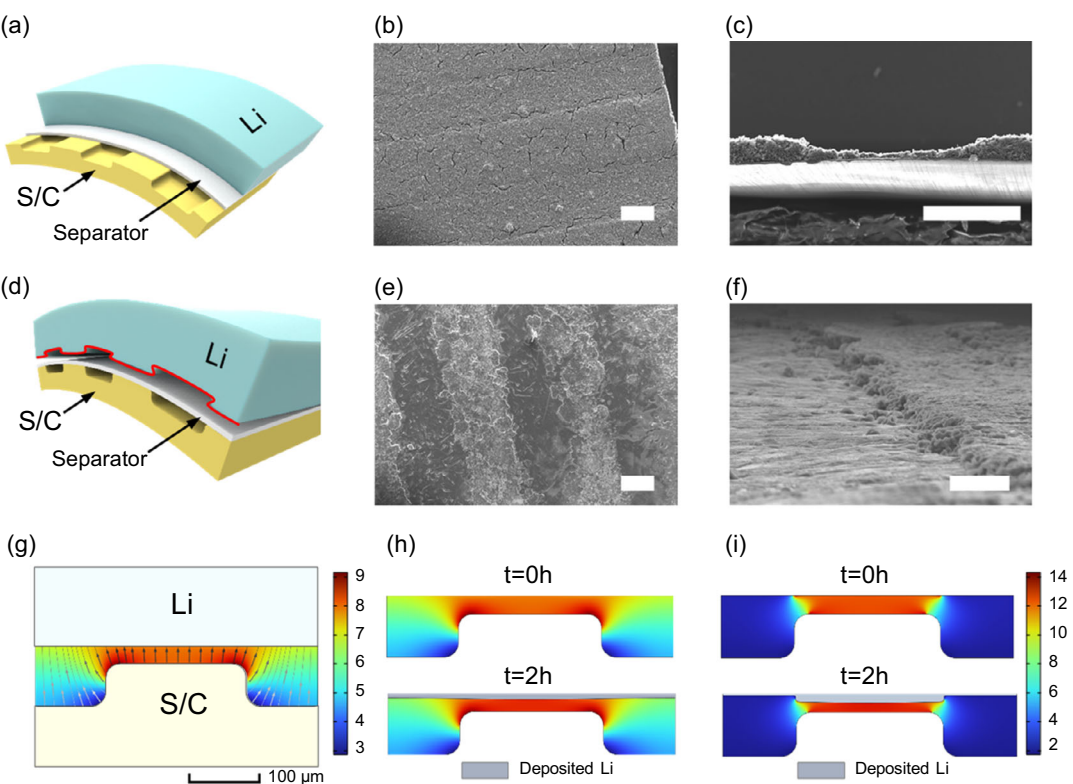


**Figure 3.** a) Schematic illustration of the corrugated S/C cathode in a cell. SEM images of the corrugated S/C cathode: b) top view and c) cross-sectional view. d) Schematic illustration of the corrugated Li anode formed after cycling (three cycles at 0.1 C). SEM images of the corrugated Li anode: e) top view and f) oblique view. The scale bars are 0.5 mm for (b), (c), and (e), and 100  $\mu$ m for (f). COMSOL simulations of the above corrugated electrode include g) current density distribution in the electrolyte region with arrows indicating the direction of Li ion migration, h) Li deposition simulation under the given framework, and i) Li deposition with the exchange current density in the recessed regions of the cathode and the corresponding areas of the anode reduced by a factor of 5. In (g–i), different colors represent local current density values, with units of  $A \cdot m^{-2}$ .

experimental results in Figure 3e,f. SEM analysis reveals that lithium plating is highly concentrated in the specific regions on the anode opposite to the protrusions, while other areas show almost no deposition. This simulated result can be reasonably understood, as a closer examination of the current density distribution across the anode surface shows an  $\approx$ 1.2-fold difference in current density (Figure S22, Supporting Information). According to Faraday's law, the discrepancy in lithium plating thickness should theoretically correspond to this 1.2-fold difference. Overall, the preferential lithium plating on the anode cannot be fully accounted for by the nonuniform current density merely arising from electrode surface topography. In the following we therefore consider a refined model.

Above we focused on investigating ion diffusion and electromigration within the electrolyte while assuming the exchange current density at the electrode surfaces to be uniform and constant. However, questions remain regarding the true uniformity of the exchange current density. Postcycling analysis of the structural transformation that occurs in the cathode reveals distinct differences in chemical environments between the raised and recessed regions, which could influence the exchange current density in these areas (Figure S23–S25, Supporting Information). Moreover, heterogeneity in the solid electrolyte interphase (SEI) layer on the lithium anode further influences the exchange current density on its surface. Therefore, under actual conditions,

the exchange current density across both the cathode and anode surfaces is inherently nonuniform. As shown in Figure 3i, reducing the exchange current density at the recessed regions of the cathode and the corresponding areas on the anode in simulations lead to lithium deposition becoming more concentrated in specific regions. This simulated outcome closely mirrors the phenomena observed experimentally. Thus, the "imprinting effect" is not solely a consequence of nonuniform current density distribution due to topography but also reflects the impact of uneven exchange current density across electrode surfaces.

Building on our findings that the cathode topography induces an imprinting effect, we hypothesize that a rough cathode surface could disrupt current distribution and lead to a localized high current density, thus increasing the risk of lithium dendrite growth and subsequent short-circuiting. To further explore whether surface roughness directly contributes to overcharging failure, we prepared two C/S cathodes with identical composition but distinctly different roughness levels by slightly altering the blade-coating process, as shown in Figure 4a–b and S26–S27, Supporting Information. Their overcharging behaviors are then evaluated through electrochemical performance tests to validate this hypothesis.

Interestingly, the results turned out to be inconsistent with the expected outcome. As shown in Figure 4c,d and S28–S29, Supporting Information, flat electrodes deliver higher capacities,

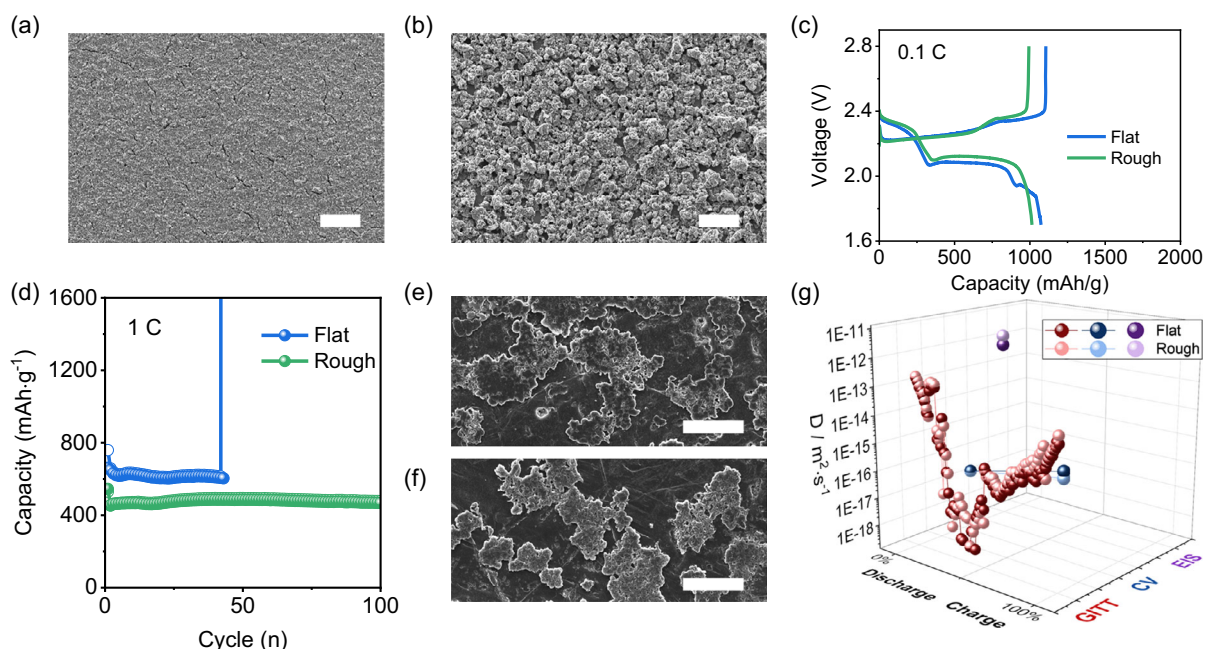


**Figure 4.** a) SEM images of the flat and b) rough S/C cathodes with the same material and loading. c) Initial discharge–charge curves of flat and rough S/C electrodes at 0.1 C. d) Cyclic performance of flat and rough electrodes at 1 C. Localized lithium plating morphologies paired with the e) flat electrode and f) rough electrode, indicating a similar plating mode. The scale bar for (a), (b), (e), and (f) are 200  $\mu\text{m}$ . g) Comparison of lithium-ion diffusion efficiency for flat and rough electrodes using different testing methods (GITT, CV, and EIS).

likely due to their smaller particle size. However, overcharging is consistently more frequent with the flat electrode group, while rough electrodes rarely exhibit such behavior. This may appear contradictory at first glance, while it reflects the complexity of the system and has prompted us to refine our understanding of influencing factors.

When we analyze the impact of current density distribution caused by surface topography, the variation in current density across the anode surface is found to be less significant (Figure S30, Supporting Information). Instead, the bulk electrode morphology may play a larger role in causing the nonuniform current density distribution, such as the smoothness or connectivity of  $\text{Li}^+$  transport pathways. In the last section, the variations of exchange current density in corrugated electrodes have also been linked to preferential Li deposition, which highlights the importance of bulk electrode properties over surface features. Figure 4c also offers some clues, the flat electrode exhibited an abnormally lower initial discharge plateau, which may be attributed to poor initial pore connectivity in the cathode.

The distribution of active material in the cathode and the lithium plating behavior at the anode are examined to evaluate reaction uniformity, with the results presented and discussed in Figure S31–S34, Supporting Information. It is worth noting that the findings reveal significant macroscopic differences in lithium plating behavior despite similar microscopic morphologies for both electrodes (Figure 4e,f). In cells with flat electrodes, the lithium plating on the anode is localized, concentrating in specific regions, which increases the risk of dendrite growth. In contrast, cells with rough electrodes exhibit more uniform lithium plating on the anode, reducing the likelihood of dendrite formation and providing greater stability (Figure S34, Supporting

Information). Electrochemical measurements were also conducted to compare the impedance and  $\text{Li}^+$  diffusion efficiency of the two electrodes which are discussed in the supplementary information (Figure S35–S37, Supporting Information) and also shown in Figure 4g. Nevertheless, the results indicate no significant differences in these parameters. Thus, the distinction between flat and rough electrodes lies in macroscopic localized variations rather than specific parameter values across the entire electrode. The porous and highly connected structure of the rough electrode may facilitate more uniform participation in electrochemical reactions, thereby mitigating the occurrence of overcharging.

Overall, the overcharging mechanism appears to arise from a combination of factors. Inhomogeneities in the cathode, such as variation in the micro- or macrostructure and differences in sulfur distribution, lead to disparities in electrochemical activity and Li-ion flux. As dendrite growth theory suggests, when certain regions on the lithium anode surface reach the limiting current density (LCD), lithium growth transitions into a unidirectional mode, a phenomenon known as Sand's time.<sup>[10]</sup> Local nonuniformities increase the likelihood of some regions reaching the LCD, triggering ISCs. Due to the inherently irregular and fragmented nature of dendrite growth, these short circuits are dynamic, with connections continuously breaking and reforming. This phenomenon, often referred to as soft short circuits, ultimately leads to overcharging failure. This process is illustrated in Figure 5a,b. Notably, previous *in situ* studies under lithium dendrite-induced short-circuit conditions have reported both the repeated formation and disconnection of lithium structures, resembling a fuse-like effect, and ongoing internal redox reactions at the cathode.<sup>[11,7a]</sup> These observations are consistent with

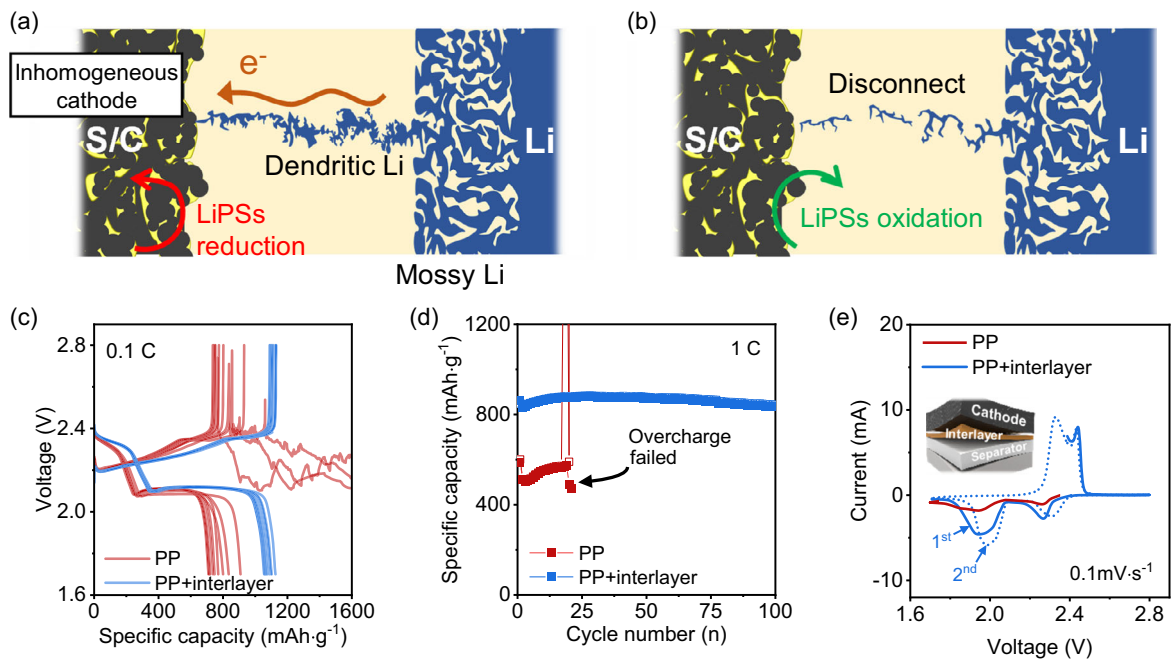


**Figure 5.** a,b) Schematic illustrations of overcharging failure caused by soft ISC. c) Charge–discharge profiles at 0.1 C under sulfur loading of  $3.5 \text{ mg cm}^{-2}$ , d) cycling performance at 1 C, and e) CV curves of cells with bare PP and SuperP-based interlayer-modified PP separators.

the dynamic short-circuiting mechanism proposed in this work. In addition, thermal effects were also observed during overcharging in some cases, as evidenced by the melting of the aluminum current collector on the cathode after severe overcharging (Figure S38, Supporting Information). This indicates that such overcharging failures pose potential safety risks associated with thermal runaway.

Additionally, polysulfide dissolution and the associated shuttle effect, while not directly responsible for triggering overcharging failure, may indirectly intensify internal inhomogeneities. Specifically, uneven polysulfide dissolution and redeposition processes can exacerbate localized variations in cathode morphology and alter SEI characteristics on the lithium anode, thus amplifying the conditions favorable for dendrite-induced short circuits.<sup>[12]</sup>

To prevent overcharging, achieving a homogeneous cathode with a well-connected structure is essential. Another potential approach is the use of a homogeneous interlayer placed between the cathode and the separator. As shown in Figure 5c–e, inserting a SuperP interlayer between the S/C cathode and the separator significantly mitigates overcharging. Moreover, both the capacity and cycling stability are greatly improved. For a sulfur loading of  $3.5 \text{ mg cm}^{-2}$ , the initial capacity at 0.1C increases from 909 to  $1126 \text{ mAh g}^{-1}$  with the insertion of the interlayer, and the subsequent cycling curves also become more stable (Figure 5c). During 1C cycling, the bare PP-based cell experiences severe overcharging within 20 cycles. Instead, the electrodes from the same batch show significantly improved capacity and cyclic reliability with the SuperP interlayer (Figure 5d). The cyclic voltammetry (CV) curves further highlight the differences between the two (Figure 5e). The bare PP cell exhibits a sharp rise in the oxidation curve, indicating short circuit. In contrast, the cell with the

interlayer demonstrates a complete CV curve, with more distinct redox peaks and reduced polarization, suggesting higher sulfur utilization.

To analyze the underlying mechanism, a schematic of the surface roughness view is presented in Figure S39, Supporting Information. The SuperP interlayer acts as an extension of the cathode, contributing to numerous active sites for the conversion and deposition of lithium polysulfides. This allows it to effectively capture dissolved lithium polysulfides, significantly enhancing the sulfur utilization. Additionally, as the interlayer seamlessly covers the cathode surface, it subtly modifies the overall topography, thereby reducing the uneven effects caused by surface irregularities. Furthermore, the SuperP interlayer, composed of agglomerated nanoscale particles, forms an isotropic and intricately connected porous conductive network (Figure S40, Supporting Information). This structure remains intact after prolonged cycling and effectively captures polysulfides, as demonstrated in Figure S41–S42, Supporting Information. Its homogeneous porous architecture and interaction with lithium ions help regulate ion transport pathways, smoothing the flux and promoting overall reaction uniformity. Consequently, incorporating an efficient and homogeneous region into an otherwise inhomogeneous cathode surface offers a compelling strategy for addressing these challenges. These findings underscore the critical role of efficient interlayer designs in mitigating overcharging and enhancing battery performance.

### 3. Conclusion

In this study, overcharging failure in Li-S batteries is systematically investigated. We demonstrate that overcharging is caused by ISCs due to excessive lithium dendrite growth. These short

circuits are dynamic, referred to as "soft short circuits," which intermittently connect and disconnect the cathode and anode, causing voltage fluctuations. During this process, the sulfur cathode undergoes repetitive localized charge-discharge events involving polysulfide reduction and oxidation. Postmortem analysis of an overcharged battery reveals that the sulfur cathode surface is covered by a mixed byproduct of reduced lithium sulfides and metallic lithium, which can be "cleared" through electrochemical means. Moreover, we reveal that these short circuits are typically triggered by the sulfur cathode. The inherent inhomogeneity of the sulfur cathode induces localized variations of the surface chemistry and electrochemical parameters on the lithium anode. This imbalance concentrates the current density in specific regions, eventually reaching the critical threshold known as the Sand's time. Furthermore, we demonstrate that inserting an efficient interlayer between the cathode and separator significantly reduces the risk of overcharging failure. This approach offers a practical strategy to mitigate soft short circuits, paving the way for safer battery designs.

## Acknowledgements

The authors acknowledge the financial support from the Swiss National Science Foundation via the Southeast Asia-Europe Joint Funding Scheme 2020 (grant no. IZJFZ2\_202476) and the National Science Foundation of China (grant nos. 22479101 and 00301054A1073) and of Sichuan province (grant no. 2024NSFSC0233).

## Conflict of Interest

The authors declare no conflict of interest.

## Author Contributions

**Shungui Deng:** conceptualization (equal); formal analysis (lead); investigation (lead); methodology (equal); writing—original draft (lead). **Mohammad Jafarpour:** formal analysis (supporting); investigation (supporting); writing—review and editing (supporting). **Frank Nüesch:** investigation (equal); methodology (equal); supervision (equal); writing—review and editing (equal). **Chuanfang Zhang:** conceptualization (lead); formal analysis (supporting); funding acquisition (equal); methodology (equal); project administration (supporting); supervision (equal); writing—review and editing (equal). **Jakob Heier:** conceptualization (equal); funding acquisition (lead); project administration (lead); resources (equal); supervision (equal); writing—review and editing (equal).

## Data Availability Statement

The data that support the findings of this study are available from the corresponding author upon reasonable request.

**Keywords:** Li–S batteries · lithium dendrite growth · overcharging failure · soft internal short circuits

- [1] a) H. J. Peng, J. Q. Huang, X. B. Cheng, Q. Zhang, *Adv. Energy Mater.* **2017**, *7*, 1700260; b) A. Manthiram, Y. Z. Fu, S. H. Chung, C. X. Zu, Y. S. Su, *Chem. Rev.* **2014**, *114*, 11751; c) X. Chen, T. Z. Hou, K. A. Persson, Q. Zhang, *Mater. Today* **2019**, *22*, 142; d) P. G. Bruce, S. A. Freunberger, L. J. Hardwick, J. M. Tarascon, *Nat. Mater.* **2012**, *11*, 19.
- [2] a) Y. S. Ye, F. Wu, Y. T. Liu, T. Zhao, J. Qian, Y. Xing, W. L. Li, J. Q. Huang, L. Li, Q. M. Huang, X. D. Bai, R. J. Chen, *Adv. Mater.* **2017**, *29*, 1700598; b) Y. Guo, Z. Q. Jin, J. H. Lu, L. Wei, W. K. Wang, Y. Q. Huang, A. B. Wang, *Energy Environ. Sci.* **2023**, *16*, 5274; c) Q. Cheng, Z. X. Chen, X. Y. Li, L. P. Hou, C. X. Bi, X. Q. Zhang, J. Q. Huang, B. Q. Li, *J. Energy Chem.* **2023**, *76*, 181; d) Z. N. Li, I. Sami, J. U. Yang, J. T. Li, R. V. Kumar, M. Chhowalla, *Nat. Energy* **2023**, *8*, 84.
- [3] a) Z. W. Zhang, H. J. Peng, M. Zhao, J. Q. Huang, *Adv. Funct. Mater.* **2018**, *28*, 1707536; b) S. G. Deng, T. Z. Guo, J. Heier, C. F. Zhang, *Adv. Sci.* **2023**, *10*, 2204930; c) X. Y. Tao, J. G. Wang, C. Liu, H. T. Wang, H. B. Yao, G. Y. Zheng, Z. W. Seh, Q. X. Cai, W. Y. Li, G. M. Zhou, C. X. Zu, Y. Cui, *Nat. Commun.* **2016**, *7*, 11203; d) X. L. Ji, K. T. Lee, L. F. Nazar, *Nat. Mater.* **2009**, *8*, 500. e) S. G. Deng, W. W. Sun, J. W. Tang, M. Jafarpour, F. Nüesch, J. Heier, C. F. Zhang, *Nano-Micro Lett.* **2024**, *16*, 229; f) S. Maiti, M. T. Curnan, K. Kim, K. Maiti, J. K. Kim, *Adv. Energy Mater.* **2024**, *14*, 2401911.
- [4] a) C. X. Dong, C. N. Ma, C. Zhou, Y. K. Yu, J. J. Wang, K. S. Yu, C. L. Shen, J. P. Gu, K. J. Yan, A. Zheng, M. J. Gong, X. Xu, L. Q. Mai, *Adv. Mater.* **2024**, *36*, 2407070; b) S. Lv, X. K. Ma, S. W. Ke, Y. D. Wang, T. R. Ma, S. Yuan, Z. Jin, J. L. Zuo, *J. Am. Chem. Soc.* **2024**, *146*, 9385; c) X. T. Zuo, L. F. Wang, M. M. Zhen, T. T. You, D. P. Liu, Y. Zhang, *Angew. Chem. Int. Ed.* **2024**, *63*, e202408026; d) H. Li, M. Y. Chuai, X. Xiao, Y. Y. Jia, B. Chen, C. Li, Z. H. Piao, Z. J. Lao, M. T. Zhang, R. H. Gao, B. K. Zhang, Z. Y. Han, J. L. Yang, G. M. Zhou, *J. Am. Chem. Soc.* **2023**, *145*, 22516.
- [5] R. Li, Y. J. Zeng, L. Song, J. L. Lv, C. Wang, C. A. Zhou, S. C. Cai, T. Chen, S. W. Yue, K. Ma, H. R. Yue, *Small* **2024**, *20*, 2305283.
- [6] L. L. Shi, C. S. Anderson, L. Mishra, H. Qiao, N. Canfield, Y. B. Xu, C. Q. Wang, T. J. Jang, Z. X. Yu, S. Feng, P. M. Le, V. R. Subramanian, C. M. Wang, J. Liu, J. Xiao, D. P. Lu, *Adv. Sci.* **2022**, *9*, 2201640.
- [7] a) B. H. Song, I. Dhiman, J. C. Carothers, G. M. Veith, J. Liu, H. Z. Bilheux, A. Huq, *ACS Energy Lett.* **2019**, *4*, 2402; b) L. L. Huang, L. S. Liu, L. G. Lu, X. N. Feng, X. B. Han, W. H. Li, M. X. Zhang, D. S. Li, X. B. Liu, D. U. Sauer, M. G. Ouyang, *Int. J. Energy Res.* **2021**, *45*, 15797; c) Z. H. Gong, J. L. Sun, H. B. Wang, G. Han, H. Liu, B. T. Qin, *J. Energy Storage* **2024**, *93*, 112411; d) Z. X. Chai, J. Q. Li, Z. M. Liu, Z. N. Liu, X. Jin, *Sci. Rep.* **2024**, *14*, 8673.
- [8] a) S. Menkin, J. B. Fritzke, R. Larner, C. de Leeuw, Y. Choi, A. B. Gunnarsdottir, C. P. Grey, *Faraday Discuss.* **2024**, *248*, 277; b) M. J. Counihan, K. S. Chavan, P. Barai, D. J. Powers, Y. P. Zhang, V. Srinivasan, S. Tepavcevic, *Joule* **2024**, *8*, 64.
- [9] Z. X. Chen, Q. Cheng, X. Y. Li, Z. Li, Y. W. Song, F. R. Sun, M. Zhao, X. Q. Zhang, B. Q. Li, J. Q. Huang, *J. Am. Chem. Soc.* **2023**, *145*, 16449.
- [10] a) P. Bai, J. Li, F. R. Brushett, M. Z. Bazant, *Energy Environ. Sci.* **2016**, *9*, 3221; b) A. Jana, R. E. García, *Nano Energy* **2017**, *41*, 552.
- [11] C. Hogrefe, T. Waldmann, M. Hözlé, M. Wohlfahrt-Mehrens, *J. Power Sources* **2023**, *556*, 232391.
- [12] a) X. B. Cheng, R. Zhang, C. Z. Zhao, F. Wei, J. G. Zhang, Q. Zhang, *Adv. Sci.* **2016**, *3*, 1500213; b) D. Aurbach, A. Zaban, Y. Gofer, Y. E. Ely, I. Weissman, O. Chusid, O. Abramson, *J. Power Sources* **1995**, *54*, 76.

Manuscript received: May 11, 2025  
Version of record online: